



## Short communication

## Micro direct methanol fuel cell with perforated silicon-plate integrated ionomer membrane

J.V. Larsen<sup>a,\*</sup>, B.T. Dalslet<sup>a</sup>, A.-C. Johansson<sup>a,b</sup>, C. Kallesøe<sup>b</sup>, E.V. Thomsen<sup>a</sup><sup>a</sup> Department of Micro- and Nanotechnology, Technical University of Denmark, DTU Nanotech, Building 345B, DK-2800 Kongens Lyngby, Denmark<sup>b</sup> Danish Technological Institute, Nano- and Microtechnology – Materials Characterization and High-Tech Production, DK-2630 Taastrup, Denmark

## H I G H L I G H T S

- We show the fabrication of a single wafer bipolar-plate micro direct methanol fuel cell.
- We show a measurement setup and model able to determine the ionic resistance through the devices.
- We examine the effects of membrane support plate geometry on device performance.
- Open circuit potential is increased at lower rates of plate perforation.
- Peak power density is increased at higher rates of plate perforation.

## A R T I C L E I N F O

## Article history:

Received 9 August 2013

Received in revised form

13 January 2014

Accepted 27 January 2014

Available online 5 February 2014

## Keywords:

Fuel cells

Methanol

Silicon

Electrochemical impedance spectroscopy

PEM

## A B S T R A C T

This article describes the fabrication and characterization of a silicon based micro direct methanol fuel cell using a Nafion ionomer membrane integrated into a perforated silicon plate. The focus of this work is to provide a platform for micro- and nanostructuring of a combined current collector and catalytic electrode. AC impedance spectroscopy is utilized alongside *IV* characterization to determine the influence of the plate perforation geometries on the cell performance. It is found that higher ratios of perforation increases peak power density, with the highest achieved being  $2.5 \text{ mW cm}^{-2}$  at a perforation ratio of 40.3%. The presented fuel cells also show a high volumetric peak power density of  $2 \text{ mW cm}^{-3}$  in light of the small system volume of  $480 \text{ }\mu\text{L}$ , while being fully self contained and passively feed.

© 2014 Elsevier B.V. All rights reserved.

## 1. Introduction

In recent times as consumer electronic devices have continued to scale down in size and increase in complexity, so has the requirements on their power-sources increased. On the typical device scale, the power requirements of mobile phones and laptops can be fulfilled to some extent with lithium ion batteries allowing modest battery lifetimes as well as easy recharging. However on the smaller device scale such as personal medical devices and hearing aids, the size requirements have made typical rechargeable batteries infeasible. These devices, which must operate at room temperature, are primarily powered by single use zinc-air batteries. This work deals with silicon based micro Direct Methanol Fuel Cells ( $\mu\text{DMFC}$ ) as a possible replacement power source for such small medical devices.

These can potentially deliver higher energy density, as well as very fast recharging through fuel exchange, which can be carried out in seconds. Methanol fuel cells work by oxidizing methanol at a catalyst layer at the anode which is typically constructed from platinum/ruthenium alloys to mitigate carbon monoxide poisoning, while oxygen is reduced at the catalyst layer at the cathode typically constructed from platinum. Silicon technology when used in  $\mu\text{DMFC}$  is typically employed to create micro-structured current collector electrodes, which are then stacked around a conventional catalyst coated proton conductive polymer layer, conventionally  $100 \text{ }\mu\text{m}$  thick Nafion 117 sheets. Such a design is termed a bipolar plate design [1]. This design is often used in active systems utilizing pumps and operating at elevated temperatures [2–4] but has also been implemented in room temperature operating passive air-breathing cells [5–7].

In this article the focus is on a novel silicon based bipolar plate design with an integrated membrane as opposed to the conventional stacked electrode design [5], for which the silicon electrodes

\* Corresponding author.

E-mail addresses: [jvila@nanotech.dtu.dk](mailto:jvila@nanotech.dtu.dk), [jackie.v.larsen@gmail.com](mailto:jackie.v.larsen@gmail.com) (J.V. Larsen).

are mechanically attached around a conventional membrane structure. The presented design allows the full cell to be defined in a single silicon wafer without need for bonding or mechanical assembly, and with the fuel reservoir attached simply through conductive adhesives or soldering.

In a review of the current state of  $\mu$ DMFC research by Sundarajan et al. [8] two major disadvantages of silicon fabrication techniques were highlighted: There is poor adhesion between the proton conductive polymer membrane and the silicon plates, and silicon is brittle making it difficult to compress the cell to lower the electrical resistance between the catalyst layers and the bipolar silicon plates.

The design presented in this work, shown in Fig. 1, addresses both of these disadvantages by integrating the ionomer membrane directly into a silicon plate structure. The problem of poor adhesion is solved by mechanical locking of the membrane into the structure such that when in a dry state the polymer is held in place mechanically, and when in a wet state the expansion of the polymer will press against the sides of the locking structure and increase the adhesion.

The problem of contact resistance is addressed by integrating the current collector electrodes into the silicon support, burying them beneath the catalyst layer. This can potentially reduce the needs for high force clamping, and allows for non-conducting materials to be used as Gas Diffusion Layers (GDL). Typically these layers must fill the role of both GDL as well as contact layer between catalyst and current collector plates, and are therefore limited to conductive materials.

## 2. Experimental

### 2.1. Micro direct methanol fuel cell design

The devices covered in this article were designed with the purpose of studying the influences of geometrical variations in a silicon plate integrated ionomer membrane, a side view is shown schematically in Fig. 1. Current collector electrodes were integrated into the silicon plate surface by deposition of 100 nm thick gold layers. The plate structure is etched into a 350  $\mu$ m thick silicon wafer, the 100  $\mu$ m thick plates are then perforated by etching a lattice structure of holes as shown in Fig. 2. The lattice spacing,  $a$ , and hole diameters,  $d$ , were then varied to study the effects of different aspect ratios with devices constructed to have 6 different geometries denoted type A–F as listed in Table 1.

The perforation ratio,  $\alpha$ , is given by the ratio of the area of three holes ( $A_h = 3\pi/4 d^2$ ) to a lattice unit cell area ( $A_{lu} = 3\sqrt{3}/2a^2$ ). Both resistance and methanol permeation will scale inversely with this active area ratio ( $\alpha = (\pi/2\sqrt{3})(d/a)^2$ ). Under the assumption that the pores defined by the holes are completely filled, the higher perforation should lead to an increased proton conductance between the anode and cathode but also an increased diffusive flow of methanol through the membrane.

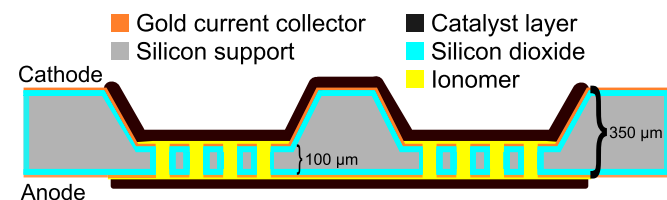


Fig. 1. Schematic illustration of the fuel cell design. The cell geometry is a bipolar plate configuration with the ionomer membrane integrated into a silicon plate structure. Elements are not to scale.

### 2.2. Fabrication of silicon plate supported fuel cell

A step by step schematic illustration of the fabrication process is shown in Fig. 3. The major elements are; definition of the supporting plates, perforation of the plates, electrode definition, ionomer integration and catalyst layer deposition. These elements are explained below with references to the step numbers in Fig. 3.

#### 2.2.1. Silicon plate defining KOH etch

In order to achieve a thin plate which still has sufficiently high mechanical strength to allow processing and dicing, KOH wet etching is used to define a recess in the wafer (step S1.1–4). Prior to etching a Low Pressure Chemical Vapor Deposition (LPCVD) silicon rich low stress nitride layer of 100 nm is deposited (S1.1). The frame mask is defined through photolithography and Reactive Ion Etching (RIE) of the silicon nitride layer (S1.2). The wafers are submerged in a 80 °C hot 28% mass fraction KOH solution for approximately 3.5 h (S1.3). The process is timed in order to create 100  $\mu$ m thick plates with the masked regions forming 350  $\mu$ m thick support frames as shown in the top part of Fig. 2. Alongside the frames, the anisotropic nature of the KOH etch is also used to simultaneously define 50  $\mu$ m wide V-groves along the boundaries of each device which serve as fracture lines during dicing. The etching of these groves self terminate at 50  $\mu$ m depth due to the highly anisotropic etch rate of KOH in silicon. These fracture lines are used as an alternative dicing method, because conventional sawing is damaging to fragile surface structures. After the etching the remaining silicon nitride is stripped in hot phosphoric acid (S1.4).

#### 2.2.2. Silicon plate perforation

The perforation of the silicon plate is carried out using Deep Reactive Ion Etching (DRIE). The etch mask is created by first depositing a 2  $\mu$ m LPCVD tetraethyl orthosilicate (TEOS) oxide layer (S2.1), which is patterned through positive photolithography (S2.2). The layer is much thicker than needed considering only etch selectivity. This is due to the simultaneous usage of the backside as a stop layer during the etch (S2.3). As such the layer is designed to be thick enough to withstand the pressure difference between the plasma chamber and the helium flow on the bottom side of the wafer which provides cooling during the etching process. It has been seen during processing that fractures can lead to the entire wafer declamping, which underlines the need for a thick oxide layer. Because the etch stops on the oxide layer charging is a potential problem which can lead to notch formations. This aspect is pronounced by the variations in geometry across the wafer which leads to large differences in etch rate. In order to ensure that the smallest features are fully etched, the larger features must be over-etched. To alleviate this problem a low frequency generator is used to remove charge during the etch process, which stops the process when the bottom oxide is reached without under-etching along this stopping layer. The oxide mask/stop-layer is then stripped in buffered HF (S2.4).

#### 2.2.3. Electrode definition

In order to prevent shorts forming between the two current collector electrodes on either side of the silicon plate, the wafers are passivated in a dry oxidation, defining a 200 nm silicon dioxide layer (S3.1). The current collector electrodes are defined by first a sputter deposition of a 10 nm thick TiW anti-diffusion barrier followed by an e-beam evaporation of 100 nm gold (S3.2). The high directionality of e-beam evaporation prevents shorts through the plate perforation holes, however in trials with larger 100  $\mu$ m holes short circuits have been observed.

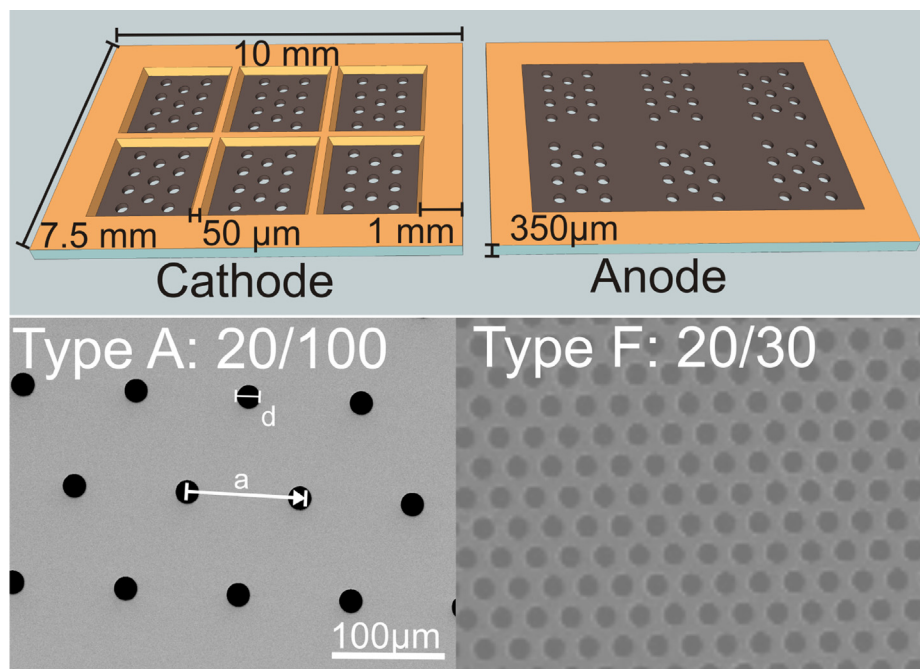


**Fig. 2.** Top) a 3D view of the anode and cathode sides of the device. The frames are shown to scale, the hole lattice is enlarged greatly to make it visible. Bottom) top view SEM image of the hole lattice for Type A and Type F devices.

#### 2.2.4. Membrane integration

The proton conducting ionomer membrane is integrated into the silicon plate using drying by evaporation from a solution under low pressure  $\approx 300$  mBar (S4.1). The geometry during the drying process is shown in Fig. 4. The drying is carried out with the finished silicon plates mounted in Polydimethylsiloxane (PDMS) molds. The dimensions of these molds critically affect the dynamics of the ionomer deposition on the plate surface.

The solution used is Nafion<sup>®</sup> DE 2020 by Sigma Aldrich consisting of 20 wt.% Nafion ion-exchange resin in lower alcohols with 34 wt.% water. Owing to the low polymer content, a direct submersion of the support structure and subsequent drying would lead to void formations as well as partially filled capillaries. In addition to this, dissolved gas would also lead to void formations during drying. In order to circumvent these problems, a method of evaporation from a slow moving surface front is utilized. Initially the Nafion solution is submerged entirely in pure isopropanol (Step 1). This delays the drying of the Nafion solution for approximately 2 h, during which the solution can thoroughly degas. After this initial delay the Nafion solution will start to dry. As the solution dries, the Nafion concentration at the drying front steadily increases until it forms a solid membrane which deposits on the edges of the PDMS holder and on the device surface (Step 2). Since the deposited Nafion membrane is permeable to the solvent, the evaporation continues to facilitate a flow of polymer to the membrane. This flow steadily increases the membrane thickness into and through the capillaries. As the drying continues through the backside of the device, the dried Nafion detaches from the solution, and gas develops on the backside of the device (Step 3). This pushes up the holder and causes the remaining ionomer solution to leak through the bottom. A critical element of the process is the thickness of the silicon plate be thin enough that this gas development process is not initiated until after the membrane has deposited through the capillaries. After the drying, the devices are annealed at 140 °C for 30 min in ambient air. The annealing process removes any solvent remains and has been shown to reduce ionic resistance and increase mechanical stability [9].

#### 2.2.5. Catalyst integration

The catalyst layer is added with spray deposition (S4.2). The final layer consists of carbon black supported catalyst particles bound by ionomer. The spray deposition solutions consisted of a dry catalyst powder dissolved in a water alcohol mixture which evaporates during the coating process. The dry powder consists of mass fractions of 70% Pt and 75% PtRu particles on the cathode side and anode side, respectively, supported on carbon black. The mixture also includes Nafion and a dispersion agent, polyvinylpyrrolidone, leading to the deposited catalyst layers having relative mass fraction loadings of 57% and 53% and catalyst loadings of 4 mg cm<sup>-2</sup> and 2 mg cm<sup>-2</sup> on the cathode and anode, respectively. To aid alcohol evaporation during spray deposition the devices are heated to 80 °C during the coating process.

#### 2.2.6. Fuel cell assembly

Finally the finished silicon device is attached to a CNC-milled brass reservoir, using a carbon based conductive adhesive. The reservoir consist of a 1 mm wall, with dimensions 10 × 7.5 × 6 mm which gives an outer volume of 375 μL and a fuel volume of 220 μL. A finished device mounted on a fuel reservoir can be seen in Fig. 5. In this configuration the reservoir acts as the cathode connection, while the edge of the device on the top acts as the cathode connection. Depending on mounting usage, an additional top casing can be fixed to the top to protect the membrane from

**Table 1**

Table of perforation lattices investigated during this work. The perforation ratio is the fraction of the proton conductive area to the catalytically active area.

Device type	Hole diameter [μm]	Lattice spacing [μm]	Perforation ratio [%]
A	20	100	3.6
B	10	60	2.5
C	10	30	10.1
D	15	45	10.1
E	10	20	22.7
F	20	30	40.3

## Plate Defining Etch

## S1.1 LPCVD Nitride



## S1.2 Photolithography &amp; RIE



## S1.3 KOH wet etch

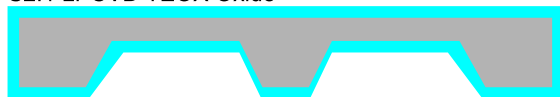


## S1.4 Nitride strip

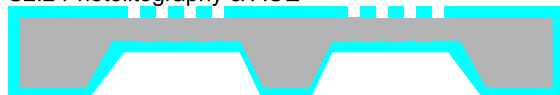


## Plate Perforation

## S2.1 LPCVD TEOS Oxide



## S2.2 Photolithography &amp; AOE



## S2.3 DRIE dry etch



## S2.4 Oxide strip

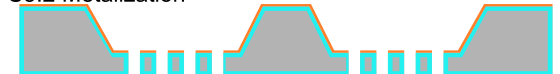


## Electrode Definition

## S3.1 Wet oxidation

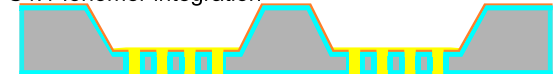


## S3.2 Metalization



## Membrane and Catalyst Integration

## S4.1 Ionomer integration



## S4.2 Catalyst deposition



Gold current collector  
 Silicon support  
 Silicon Nitride  
 Ionomer  
 Catalyst layer  
 Silicodioxide

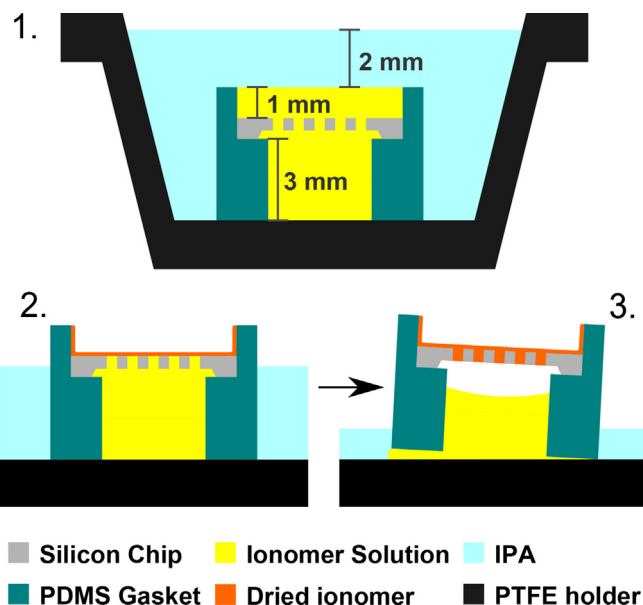


**Fig. 4.** Schematic showing the setup for the evacuated evaporation drying used to integrate the ionomer in S4.1 of the fabrication process as shown in Fig. 3.



**Fig. 5.** A finished device shown on top of a 220 µL capacity fuel reservoir shown next to a one euro coin for scale. Fuel is injected through holes in the bottom of the reservoir which are not visible.

mechanical damage. The brass reservoir has two small holes milled into the top. PDMS plugs are cast into these holes to prevent liquid from escaping. Fuel can then be added to the reservoir by puncturing both holes with syringes and adding liquid through one while letting gas escape through the other. In a similar fashion after finished operation, the remaining water and unused residual fuel can be extracted by injecting air into one syringe while letting the liquids escape through the other.

### 2.3. Characterization setups

The finalized fuel cells have been characterized using current potential sweeps to determine their external performance characteristics in form of the power density and internal resistance. Also an AC impedance spectroscopy setup was used to characterize the through device resistance, to determine the integrated membrane

**Fig. 3.** Illustration of the fabrication process flow. The process consists of two mask steps (S1.2, S2.2), passivation and metalization steps (S3.1–2) and the ionomer integration step followed by a spray coating of catalyst layers (S4.1–2). Elements are not to scale.



conductivity. In both characterization setups the measurements are carried out using reusable electrodes and the devices were tested without fuel reservoirs mounted.

### 2.3.1. Current potential characterization

The characterization of the cells was carried out by varying the drawn current and measuring the potential using a Keithley 2100 source-meter. The silicon devices are placed between two copper electrodes, and a 200  $\mu\text{L}$  reservoir filled with 3 M methanol. After the Open Circuit Potential (OCV) stabilizes, the current is swept from zero until the potential has decreased to zero at a scan rate of  $0.2 \text{ mA s}^{-1}$ . The peak power density is found by taking the maximum point in the power curve, and a measure of the total effective internal resistance ( $R_{\text{int}}$ ) is found through a least squares fit to a linear ohmic potential loss. The fit is made in the region from the peak power density and upwards in current. The performance characteristics are a complicated nonlinear system with contributions such as kinetic and mass transfer losses at both anode and cathode and ohmic losses associated with the membrane transport and electrical transport in the catalyst layers. Contact resistances between catalyst layer and collector electrode and between catalyst layers and the ionomer membrane also contribute. In addition to these, the cross-over permeation of methanol through the membrane will be driven by the concentration gradient and as such will depend on the current drawn. Due to these many contributing factors a more developed model will not adequately be able to distinguish contributions to the effective internal resistance, and a different approach is therefore pursued in order to gain an operation independent gauge of the membrane resistance, through an AC Impedance Spectroscopy measurement setup.

### 2.3.2. AC impedance spectroscopy

In order to relate the performance of the devices to a measure of the ionomer membrane conductivity, a measurement setup, based on AC impedance spectroscopy [10], was created and used to measure the ionic resistance through the devices. The setup

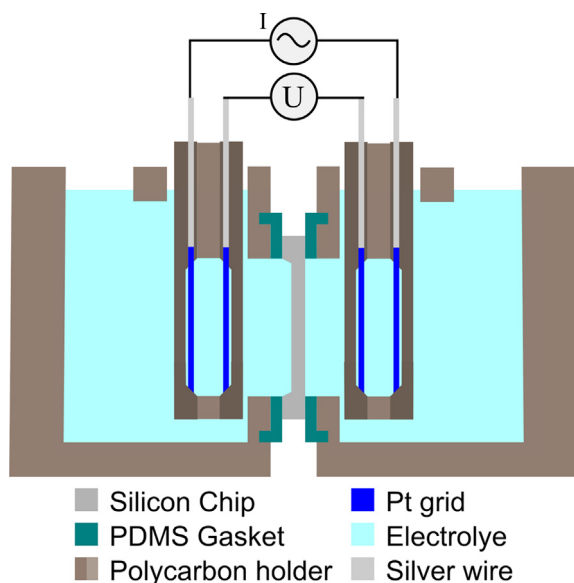


**Fig. 6.** Illustration of the measurement setup used to determine the through device resistance,  $R_{\text{td}}$ . The four platinum grid electrodes are configured in a four-point probe geometry to eliminate resistances associated with the current through the source and current collector electrodes. The electrodes are fitted into two sets of three polycarbon plates, here shown in different shades to distinguish the individual plates. (For interpretation of the references to color in this figure legend, the reader is referred to the web version of this article.)

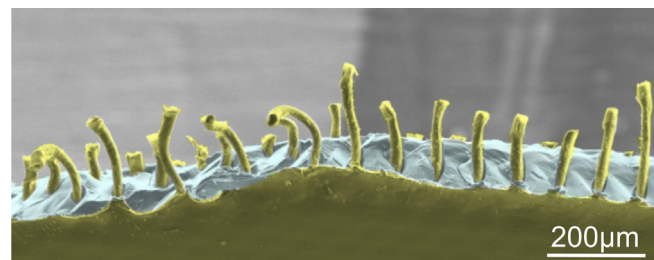


**Fig. 7.** Scanning electron microscopy image showing the ionomer integrated into the silicon plate after annealing. The ionomer is colored green against the silicon which is colored blue. The strands of ionomer were elongated during the fracture of the device, and therefore appear longer than the thickness of the plate. (For interpretation of the references to color in this figure legend, the reader is referred to the web version of this article.)

consists of two liquid reservoirs filled with 1 M sulfuric acid in water as can be seen in Fig. 6. The reservoirs are connected to the device such that it constitutes the sole conducting pathway between them. To generate and measure the electrical signals a four-point probe setup is used. Two platinum grid electrodes are situated in each reservoir clamped between polycarbonate plates. The impedance is measured using a Agilent 4294A precision impedance analyzer, with a potential signal amplitude of 100 mV rms. Since no fuel is present during these measurements, cross-over effects have no influence on the resulting spectra.

## 3. Results and discussion

### 3.1. Ionomer integration filling

A Scanning Electron Microscopy (SEM) image showing the cross section of a dried membrane can be seen in Fig. 7. The ionomer can be seen to fill the internal volume of the membrane. A thin approximately  $5 \mu\text{m}$  layer of Nafion is deposited on the bottom of the device. This side is the top side of the device illustrated in Fig. 4. The ionomer strands are longer than the membrane thickness due to being stretched during the cross-sectional fracture. The results clearly show that the ionomer integration technique utilized leads to a high filling factor integrated membrane despite the polymer only making out 20% of the initial polymer solution.

### 3.2. Power density and internal resistance

A measured  $IV$  curve for a device of type F is shown in Fig. 8. The nonlinear shape of the potential curve is due to the non-linear losses associated with the chemical overpotentials. The exact curve-shape can be fitted using more detailed models [11], however instead an effective internal resistance is found to simplify comparisons. The power densities of the studied geometries, Types A–F, are all located in the range of  $0.5\text{--}2.5 \text{ mW cm}^{-2}$ , while the open circuit potentials are in the range of  $300\text{--}470 \text{ mV}$ . The large deviation from the ideal standard potential of  $1.18 \text{ V}$  associated with the methanol oxidation reaction vs. an oxygen reduction reaction [12] is attributed to the formation of a mixed potential [13], as methanol diffuses through the membrane to the cathode side.

### 3.3. Through device resistance

Two equivalent circuit models were used to model the measured impedance data and as fitting functions. The first model is a classical Randles circuit [14] shown in Fig. 9.

The resistance of the electrolyte is described by  $R_0$ . The resistance connected in parallel,  $R_{\text{td}}$ , is the resistance through the entire

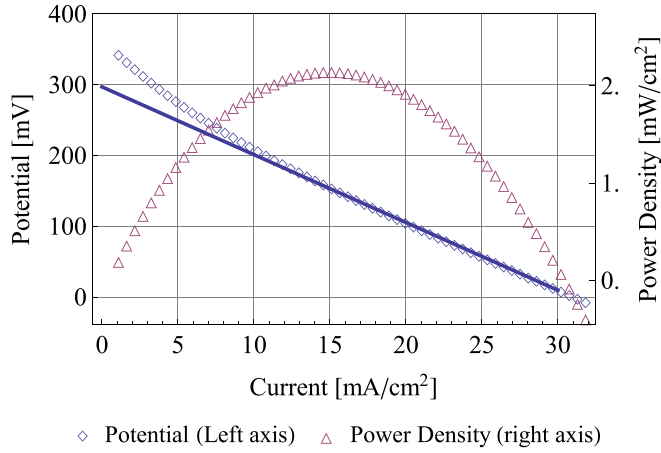


**Fig. 8.** IV curve for a Type F device with 20  $\mu\text{m}$  diameter holes with lattice spacing of 30  $\mu\text{m}$ . The peak power is found to be 2.3  $\text{mW cm}^{-2}$ . The solid line shows a linear fit used to determine an effective internal resistance which was found to be 21.77  $\Omega$  corresponding to 9.58  $\Omega \text{ cm}^{-2}$ .

device, and therefore contains both contributions from the membrane and the porous catalyst layers. The capacitive element,  $C$ , models the geometric capacitance between the two sides of the device, and the Warburg element,  $W$ , models diffusion at the sensing electrodes. The impedance of the Warburg element,  $Z_w$ , and the capacitor,  $Z_C$ , are

$$Z_w = \sqrt{2} \frac{A_w}{\sqrt{i\omega}} \quad Z_C = \frac{1}{Ci\omega}$$

where  $A_w$  is the Warburg constant,  $\omega$  the angular frequency and  $i$  the imaginary unit. The impedance of the Randles circuit is given by

$$Z_R = R_0 + \frac{1}{\frac{1}{R_{td} + Z_w} + \frac{1}{Z_C}} \quad (1)$$

The results of fitting this model to data can be seen in Fig. 10, where it is clearly shown that the model does not provide a satisfactory fit for the measured data.

The other model used is a modified Randles circuit. The Randles circuit is based on the assumption of a perfect capacitor as well as semi-infinite linear diffusion at the sensing electrodes. These assumptions are not applicable for the devices investigated, and the circuit is therefore modified to take non-ideal effects into account. Two changes are made. The Warburg element is substituted out for a constant phase element [15],  $Z_{Qw}$ , with amplitude  $W_a$  and phase angle parameter,  $n_w$ , close to the value of 1/2 that would correspond to an ideal Warburg element. The impedance is given by

$$Z_{Qw} = \frac{W_a}{(i\omega)^{n_w}}$$

Similarly the Randles circuit assumes an ideal capacitor, this assumption does not hold for these devices, since the ideal

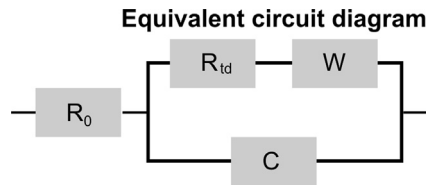


**Fig. 9.** A Randles circuit is used to model the measured impedance spectrum.  $W$  is a Warburg diffusion element and  $C$  is a capacitive element.  $R_{td}$  is the through device resistance, and  $R_0$  is the serial resistance of the connecting elements.

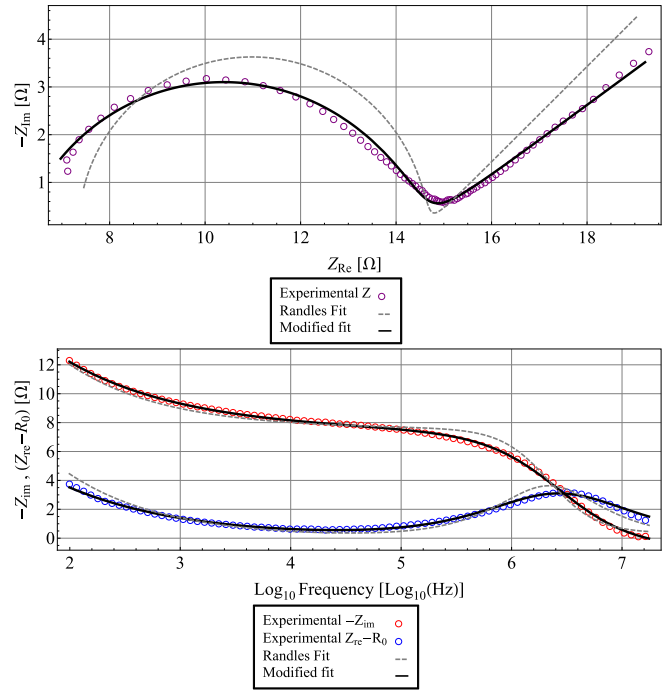


**Fig. 10.** Measured impedance across a type D device with 15  $\mu\text{m}$  holes in a 45  $\mu\text{m}$  lattice, corresponding to 10% porosity. The top part of the figure shows a Nyquist plot and the bottom part shows a Bode plot. The results of the modified Randles circuit fit is a resistance of 8.3  $\Omega$ , with an equivalent capacitance of 43.8 nF.

capacitor assumes a uniform medium and planar electrodes while the device has porous electrodes and a non uniform medium [16]. Therefore the capacitive element is replaced with a constant phase element,  $Z_{Qc}$ , with prefactor  $1/Q_c$ , and a phase angle parameter,  $n$ , close to the value of 1, which would correspond to an ideal capacitor. The impedance of this element is given by

$$Z_{Qc} = \frac{1}{Q_c} \frac{1}{(i\omega)^n}$$

Finally the impedance of the modified Randles circuit,  $Z_M$ , becomes

$$Z_M = R_0 + \frac{1}{\frac{1}{R_{td} + Z_{Qw}} + \frac{1}{Z_{Qc}}}$$

During the fitting of impedance data to the modified Randles circuit the fitted phase angles for these two constant phase elements gave results close to the ideal values. For the Warburg and capacitive elements the average fitted values are  $n_w \approx 0.32$  and  $n \approx 0.9$ , respectively.

Since the data is collected in a logarithmic frequency space,  $F = \log_{10}(\omega/2\pi)$ , during actual fitting the models are re-expressed as

$$F_0 = \log_{10}(2\pi Q_c \sqrt[n]{R_{td}}) \quad (2)$$

$$Z_M(\Omega) = R_0 + R_{td} \frac{1}{(1 + a(i10^F)^{-n_w})^{-1} + i10^{n(F-F_0)}}$$

where  $a = W_a/R_{td}$  is the normalized Warburg element amplitude, and the phase angles are fixed to  $n_w = 1/2$  and  $n = 1$  when fitting the unmodified Randles circuit.

The modified Randles model fits the data well, with the average standard error on the estimated membrane resistance  $R_{td}$  being  $\sim 0.02 \Omega$ . A Nyquist plot of fit and data for a type D device is presented in the top of Fig. 10, a Bode plot is shown in the bottom part

of the figure. The results show good agreement between data and the modified Randles circuit fit. The unmodified Randles circuit fit is also shown, and it clearly shows problems in describing the low frequency curve angle and circle suppression. In the modified Randles circuit, a systematic deviation is apparent in the low frequency side, or equivalently higher resistance side of the depressed semicircle. Here the model is defined to be symmetric about the central frequency, however a linear constant angle slope is observed in the Nyquist plot in the top of Fig. 10. An equivalent capacitance can be found for the constant phase element through  $C_{eq} = (R_{td}2\pi10^{F_0})^{-1}$  [16]. For the shown device the capacitance is found to be  $C_{eq} = 43.8$  nF, which is close to the expected range of the geometric capacitance for two  $0.44$  cm<sup>2</sup> electrodes separated by  $100$   $\mu$ m silicon assuming a relative permittivity of  $\epsilon_r = 11.6$  which is  $C_g \approx 45$  nF. The difference could be ascribed to the lower relative permittivity of the plate due to the Nafion filled pores. The resistance found through this measurement is not strictly equal to the resistance through the membrane, as conductance through the porous ionomer containing catalyst layers also contribute. It is, however, assumed that the primary contribution arises from the membrane, due to the porous volume of the catalyst layers filling with electrolyte and due to the membrane being  $100$   $\mu$ m thick vs. the  $\sim 10$   $\mu$ m thick catalyst layers.

Nafion has a conductivity which is highly dependent on hydration level, assuming a conductivity of  $\sigma \in [0.1, 0.01]$   $\Omega$ , for a membrane with area  $A = 0.44$  cm<sup>2</sup> and length,  $L = 0.1$  mm, the expected resistance is within  $R \in [0.27, 2.72]$   $\Omega$ . For an effective area of only 10%, this would lead to  $R \in [1.36, 13.62]$   $\Omega$ . For a device with an effective area ratio of  $\alpha = 10\%$  of the membrane resistance was found to be in the range of  $R_{td} \approx 15$   $\Omega$ , for the devices with a lower resistance. For a single device the resistance was observed as high as  $\approx 35$   $\Omega$ . This would suggest that the ionomer conductivity is in the lower region compared to well hydrated traditional membranes. This could be due to a lower level of hydration, perhaps impeded by the microstructure integration.

### 3.4. Influence of plate geometry on performance

A batch of 9 devices were examined, for each device the internal resistance and peak power density were found through IV characterization and the through device resistance/conductance was determined by use of AC impedance spectroscopy.

A plot of the OCV as a function of the through device resistance is shown in Fig. 11. It can be seen that the OCVs of the devices were all located in the range of 300–550 mV. Devices with higher through device resistance are seen to also have higher OCV, indicating that reduction in membrane conductivity also reduces methanol permeation. The correlation between effective internal resistances of the devices and the measured through device resistance is plotted in Fig. 12. The figure shows a linear tendency which indicates that the differences in internal resistances are largely determined by the conductivity of the ionomer and contact resistances between catalyst layers and ionomer.

Fig. 13 shows the relation between power density and the through device conductance,  $\sigma_{td} = 1/R_{td}$ . As expected a tendency of higher power density with higher conductance is observed. It is, however, apparent that devices with the same design, i.e.  $C_1$  and  $C_2$ , have large variations in conductivity indicating that the membrane quality variation for each deposition overshadows the influences of the differences in plate geometry. The relation between peak power density and perforation ratio, shown in Fig. 14, illustrate that there is only a slight trend between perforation ratio and achieved peak power density. It is observed that a larger perforation ratio leads to a higher peak power, with the best device design being type F with a perforation ratio of 40.3%. When considered in light of the open

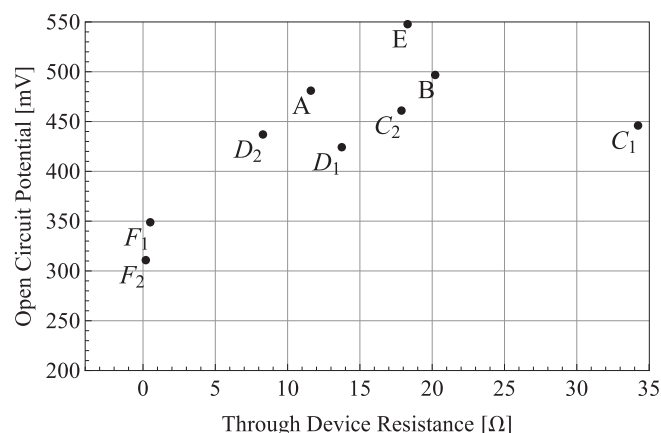


Fig. 11. Open circuit potential shown against the through device resistance ( $R_{td}$ ). All devices are shown to have OCV in the range of 300–550 mV. A tendency of higher OCV correlating to higher resistance through the device is observed.

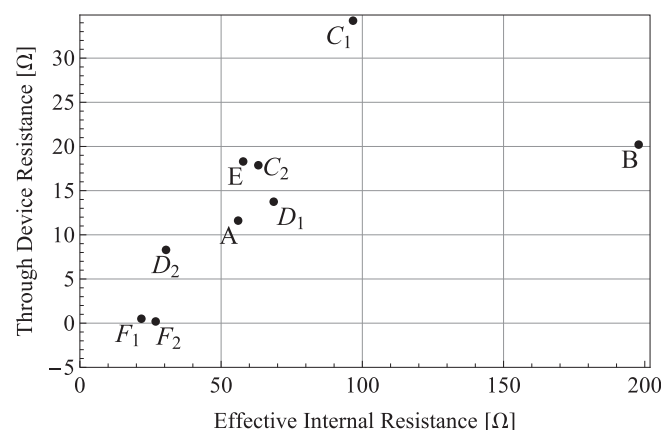


Fig. 12. Correlation between effective internal resistances ( $R_{int}$ ) of the devices and the measured through device resistance ( $R_{td}$ ). Apart from the type B device outlier, a linear trend is observed.

circuit potential drop associated with lower resistances, seen in Fig. 11, this leads to the conclusion that the performance gains associated with an increase in conductivity is greater than the loss associated with increased methanol cross-over in the devices studied.

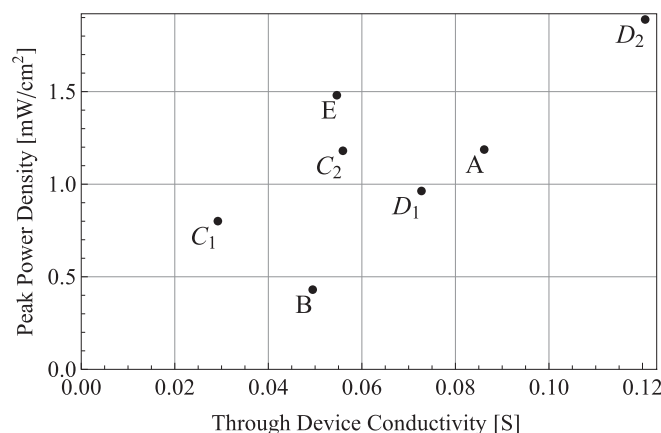
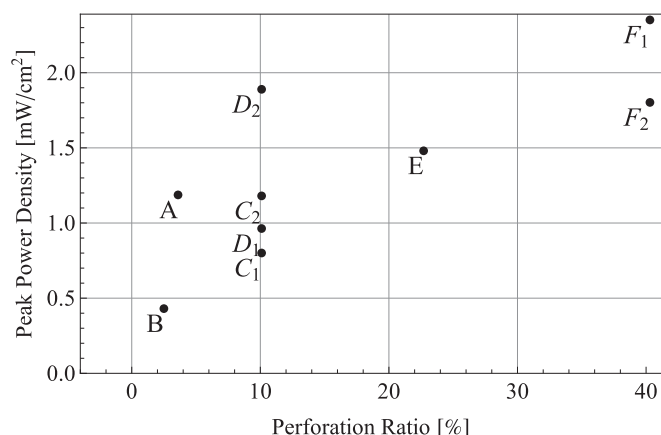


Fig. 13. Power density shown against the through device conductivity. Devices of Type F are excluded as they are an order of magnitude higher.



**Fig. 14.** Power ratio plotted against effective perforation ratio. A tendency of increased performance with higher ratios of perforation is observed. A large variation is observed between devices of similar designs and similar perforation.

### 3.5. Discussion

The performance of the fabricated devices are compared to other silicon based direct methanol fuel cell systems in Table 2. The systems are separated into passive and active categories based on the mode of operation. The table shows the peak power density per catalytic active geometric area, which shows the ability of the catalyst/membrane to deliver power. Also shown is the volumetric power density with respect to the outer system volume. The system volume is estimated from the referenced original works, and includes the mechanical structures needed to support the active cell.

The active systems utilize pumps to transport methanol to the anode, therefore their peak power densities are typically significantly higher than passive systems [2]. Especially systems utilizing an actively pumped oxygen flow are capable of achieving very high peak power density [1]. Another method often employed to increase power output is stacking multiple cells to achieve larger potentials [17,18]. Active or stacked systems have a large volume

and have been insufficient for use as power source in miniature electronic devices. Therefore it is interesting to compare the results against miniature passive fuel cell systems.

In comparison to a similar passive system by Gharibi et al. [7], the devices presented here show a higher performance with a smaller system size, and operating with open circuit potentials in a similar range, however using a higher methanol concentration. More mature systems like those presented by Ref. [6] show much larger power densities, up to  $10 \text{ mW cm}^{-2}$ , though operating at significantly larger total system sizes. It should be noted that their initial reported values were in the range of  $1\text{--}4 \text{ mW cm}^{-2}$  and only through continual optimization was the higher value obtained. In that respect the designs presented here prove interesting as the catalyst layers have yet to be optimized for the membrane configuration, while elements such as micro-porous layers also have not yet been implemented. Designs such as [5] require that the electrodes and the conventional MEA are pressed together. Therefore a large amount of the total system volume is wasted on this mechanical assembly. When comparing system sizes, it can be seen that the presented design has a much lower total system size as there is no need for mechanical assembly. Comparing the volumetric power density numbers in Table 2 it can be seen that the integrated design presented here is comparable to the stacked passive systems, while it's still somewhat below the active systems. These are however over estimates as the volume does not include the pumps needed during operation.

### 4. Conclusion

This work shows a silicon-plate integrated ionomer membrane for a passive direct methanol fuel cell. The designs were shown to lead to working fuel cells with *IV* characterization showing power densities of up to  $2.5 \text{ mW cm}^{-2}$  under passive operation at room temperature. This performance compares favorably to other reported single stack silicon based passive air-breathing DMFCs [7], but is lower than state of the art in silicon based cell [5]. The presented devices however do not require high amounts of pressure to reduce contact resistance between silicon and catalyst layers. This

**Table 2**  
Performance of different bi-polar plate designs compared to the integrated membrane of this work. The area used for the peak power density is the geometric area of the catalytic region. *T* is the operating temperature and RT denotes room temperature conditions. *C<sub>M</sub>* denotes the methanol fuel concentration used. A and C denote the anode and cathode loadings of PtRu and Pt, respectively.

Work	System size	Active area [cm <sup>2</sup> ]	Peak power density [mW cm <sup>-2</sup> ]	Volumetric peak power density [mW cm <sup>-3</sup> ]	OCV [mV]	<i>T</i> [°C]	<i>C<sub>M</sub></i> [M]	Catalyst loading [mg cm <sup>-2</sup> ]
<b>Active systems</b>								
Kelley et al. <sup>a</sup> [1]	3 cm <sup>2</sup> × 1 cm	0.25	60	5.0	700	70	0.5	A: ~2 C: 1.5
Liu et al. [4]	1 cm <sup>2</sup> × 0.5 cm	1	4.7	9.4	450	RT	2	A: 2 C: 1
Seo et al. [3]	3.5 cm <sup>2</sup> × 1 cm	1	0.031	0.000078	650	RT	1	NA
<b>Passive systems</b>								
Hashim et al. <sup>b</sup> [19]	7.5 cm <sup>2</sup> × 5 cm	4	12	0.32	2500	RT	4	A: 4 C: 2
Chan et al. <sup>b</sup> [18]	~30 cm <sup>2</sup> × 4 cm	6.25	10.3	0.54	2900	70	6	A: 4 C: 2
Shimizu et al. [6]	49 cm <sup>2</sup> × 4 cm	36	10	1.84	550	RT	4	A: 2.5 C: 2.6
Sabate et al. [5]	6 cm <sup>2</sup> × 1 cm	0.25	10	0.42	450	RT	2	A: 4 C: 4
Gharibi et al. [7]	4.75 cm <sup>2</sup> × 3 cm	4.75	1.2	0.40	500	RT	1	A: 1 C: 3
This work	0.75 cm <sup>2</sup> × 0.7 cm	0.44	2.5	2.01	500	RT	3	A: 4 C: 2

<sup>a</sup> Oxygen feed.

<sup>b</sup> Stacked system.



allows them to operate with a much smaller total system volume, and the present work reports a volumetric power density of up to  $2.5 \text{ mW cm}^{-3}$ , which is superior to similar passive systems [19,20,6,5,7] and compares favorably to active systems even when not accounting for the volume taken up by their pumping systems [1,4]. The low potential ranges compared to ideal cases are assumed to be primarily due to cross-over effects which reduce the cathode potential and also lead to a continual loss of fuel as it diffuses directly through the membrane. The exact level of the effect has not yet been investigated but is of major concern both with respect to improving IV-performance, but as important with respect to attainable energy capacity.

The devices were analyzed using AC impedance spectroscopy, which revealed a large geometry independent variation in the through device conductivity, indicating that the membrane integration is a critical fabrication step, which still needs improvement to ensure the deposited membrane conforms reproducibly to the underlying perforation geometry.

A tendency of increasing OCV associated with an increase in the membrane resistance was observed. The corresponding lower conductivity and associated ohmic losses however showed that the constriction did not provide a net performance gain. The highest performances were thus seen at the devices with the highest ratio of perforation.

In conclusion, the methodology does not show improved performance with respect to power density of the active area in current results, but fares positively in comparison considering the total device size. In addition to this, the novel design opens the possibility for micro- and nano-structured integrated catalyst layers and is interesting as a platform for further novel optimizations that can be realized by bottom up fabrication of elements such as catalyst support layers.

## Acknowledgment

The present work was supported by the Danish National Advanced Technology Foundation, under the project; “MicroPowerDK”.

## References

- [1] S.C. Kelley, G.A. Deluga, W.H. Smyrl, *AIChE J.* 48 (5) (2002) 1071–1082.
- [2] Chan Kim, Yong Jung Kim, Yoong Am Kim, Takashi Yanagisawa, Ki Chul Park, Morinobu Endo, Mildred S. Dresselhaus, *J. Appl. Phys.* 96 (10) (November 2004) 5903–5905.
- [3] Young Ho Seo, Young-Ho Cho, *Sens. Actuators A Phys.* 150 (1) (March 2009) 87–96.
- [4] Xiaowei Liu, Chunguang Suo, Yufeng Zhang, Xilian Wang, Chi Sun, Ling Li, Lifang Zhang, *J. Micromech. Microeng.* 16 (9) (September 2006) S226–S232.
- [5] N. Sabate, J.P. Esquivel, J. Santander, N. Torres, I. Gracia, P. Ivanov, L. Fonseca, E. Figueras, C. Cane, in: 2008 2nd European Conference Exhibition on Integration Issues of Miniaturized Systems – MOMS, MOEMS, ICS and Electronic Components (SSI), 2008, pp. 1–4.
- [6] Takahiro Shimizu, Toshiyuki Momma, Mohamed Mohamedi, Tetsuya Osaka, Srinivasan Sarangapani, *J. Power Sources* 137 (2) (October 2004) 277–283.
- [7] Hussein Gharibi, Farhad Golmohammadi, Mehdi Kheirmand, *Electrochim. Acta* 89 (February 2013) 212–221.
- [8] Subramanian Sundarajan, Suleyman I. Allakhverdiev, Seeram Ramakrishna, *Int. J. Hydrogen Energy* 37 (10) (May 2012) 8765–8786.
- [9] Xiaoyu Ding, Sima Didari, Thomas F. Fuller, Tequila A.L. Harris, *J. Electrochem. Soc.* 160 (8) (January 2013) F793–F797.
- [10] N. Wagner, W. Schnurnberger, B. Müller, M. Lang, *Electrochim. Acta* 43 (24) (August 1998) 3785–3793.
- [11] Brenda L. Garcia, Vijayanand Sethuraman, John W. Weidner, Roger Dougal, Ralph E. White, *Mathematical Model of a Direct Methanol Fuel Cell*, May 2004. Technical report.
- [12] JiuJun Zhang, Hansan Liu (Eds.), *Electrocatalysis of Direct Methanol Fuel Cells*, first ed., Wiley-VCH, October 2009.
- [13] Fuqiang Liu, Chao-Yang Wang, *J. Electrochem. Soc.* 154 (6) (June 2007) B514–B522.
- [14] J.E.B. Randles, *Discuss. Faraday Soc.* 1 (0) (January 1947) 11–19.
- [15] C. Criado, P. Galán-Montenegro, P. Velásquez, J.R. Ramos-Barrado, *J. Electroanal. Chem.* 488 (1) (June 2000) 59–63.
- [16] G.J. Brug, A.L.G. van den Eeden, M. Sluyters-Rehbach, J.H. Sluyters, *J. Electroanal. Chem. Interfacial Electrochem.* 176 (1–2) (September 1984) 275–295.
- [17] M.M. Ahmad, S.K. Kamarudin, W.R.W. Daud, Z. Yaakub, *Energy Convers. Manag.* 51 (4) (April 2010) 821–825.
- [18] Y.H. Chan, T.S. Zhao, R. Chen, C. Xu, *J. Power Sources* 178 (1) (March 2008) 118–124.
- [19] N. Hashim, S.K. Kamarudin, W.R.W. Daud, *Int. J. Hydrogen Energy* 34 (19) (October 2009) 8263–8269.
- [20] B.D. Cahan, J.S. Wainright, *J. Electrochem. Soc.* 140 (12) (December 1993) L185–L186.